

Research Article

Effect of Threshold Pressure Gradients on Control Areas Determination of Production Well in CBM Reservoirs

Ruifei Wang,¹ Jiaosheng Yang ,² Meizhu Wang,² Yang Zhao,² and Weiqing Chen³

¹School of Petroleum Engineering, Xi'an Shiyou University, Xi'an, China

²China National Petroleum Corporation Research Institute of Science and Technology Co., Ltd., China

³College of Petroleum Engineering & Geosciences, King Fahd University of Petroleum & Minerals (KFUPM), Dhahran, Saudi Arabia

Correspondence should be addressed to Jiaosheng Yang; yangjs6699@gmail.com

Received 4 June 2019; Revised 11 August 2019; Accepted 29 August 2019; Published 18 December 2019

Guest Editor: Mohamed M. Chehimi

Copyright © 2019 Ruifei Wang et al. This is an open access article distributed under the Creative Commons Attribution License, which permits unrestricted use, distribution, and reproduction in any medium, provided the original work is properly cited.

Understanding the mechanism of water drainage and gas recovery is the burning issue for Coalbed Methane (CBM) reservoir development. In the process of exploitation, threshold pressure gradients (TPG) is an important factor affecting the control areas, which related to the low-permeability and complex water saturation of CBM reservoirs. In this paper, a new flow model of CBM has been established considering the TPG and gas desorption. Then we carried out a series of experiments and fitted out a new relational expression between TPG and permeability and water saturation, which shows that TPG is negatively correlated with permeability and positively correlated with water saturation. After that, we analyzed the influence of TPG and desorption on the control radius and illustrated a case study. The results show that TPG and desorption effect both can slow down the rate of pressure reduction. The case study indicates that the control radius of target well groups ranges from 55 m to 136.7 m. The average control radius and gas TPG are 91.3 m 0.0082 MPa/m respectively. Furthermore, we classify the wells into 5 categories, which are mainly distributed in III (80~100 m). Finally, we suggest using well pattern infilling in region II and III and hydraulic fracturing method for region IV to increase the utilization area and the sustainability for the target area. This study provides a quick and reasonable prediction of control radius in CBM reservoir with different water saturation for further adjustment suggestion and sustainable development.

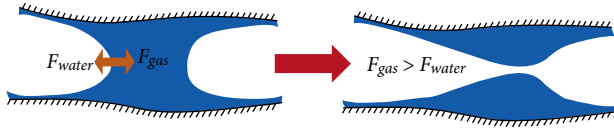
1. Introduction

In recent years, coalbed methane (CBM), as an unconventional and clean natural gas resource, has received lots of attention. The effective exploitation of CBM is of great significance to the full utilization of energy, the improvement of energy structure, and the sustainable development of energy [1, 2]. Meanwhile, the successful CBM recovery can help reduce the risk of the mine explosion and mitigate the greenhouse effect induced by the methane emission, which can achieve the sustainable development of environment and energy [3–9].

Among the researches on the CBM development, the coal is usually characterized as a dual-porosity system [10, 11], which refers to a matrix-cleat system. The coal matrix, as the primary porosity system, is comprised of micropores and stores 70–95% of total gas in the adsorbed form [12]. The cleat system, on the other hand, is composed of macropores and usually saturated with water [13, 14]. By pumping out water from cleats,

the formation pressure of coalbed will decrease, which results in the desorption of CBM and triggers its flow. With the continuous drainage, the relative permeability of water in coal seam decreases, and the relative permeability of gas increases. The water production of CBM wells decreases gradually, while gas production increases gradually and tends to be stable. Therefore, the main production stage of coalbed methane wells is gas–water two-phase flow, whose duration determines the economic benefits of the whole coalbed methane wells.

Up to now, many models have been established to study the CBM development. Some researchers focus on the production characteristics or behavior of CBM reservoirs. Zhao et al. investigated the influence of six factors on gas production quantitatively based on the grey system theory, and then put forward the optimum development strategy for CBM reservoirs in terms of those factors [15]. Lv et al. studied the temporal and spatial production characteristics of CBM wells to determine the dominant factors by using bivariate



F_{water} and F_{gas} are the interaction between gas and water

FIGURE 1: Gas transport mechanism in pores of CBM reservoirs containing water.

correlation analysis and gray system theory [16]. Wang et al. set up a numerical model to investigate the combined effect of directional compaction, nondarcy flow and anisotropic swelling on well production rates [17]. Gong et al. proposed a new workflow to perform a 2-D coalbed methane recovery simulation with a discrete fracture model to better simulate the distribution of actual cleats. They then utilized this workflow model to study the enhancement of methane recovery when injecting CO_2 [18]. Vishal et al. set up a numerical model to investigate the role of sorption time in the production behavior of CBM under carbon dioxide injection [19].

At the same time, some scholars pay more attention to the flow mechanism of gas using model establishment [20–23]. Liu et al. proposed a new semi-empirical model for describing the entire methane diffusion process, which is more effective in describing non-linear gas diffusion behavior in the coal matrix than the Fick model for the studied coals [24]. Pillalamarry et al. used a unique model to evaluate the sorption and diffusion properties of methane and study the relationship between the diffusion coefficient and pressure. Sun et al. proposed a semi-analytical model to quantify the effective gas/water phase permeability and analyze the effect of critical desorption pressure, gas desorption capacity, stress dependence, and matrix shrinkage on effective permeability [25].

Pore analysis shows that the pore size of the CBM reservoir is mainly nano/micro-scale. The interfacial effects will be obvious at this scale, and a stable adsorption water film will be formed on the solid wall, even the whole pore. The existence of water in the CBM pores will increase the flow resistance and weaken the slippage effect of the gas, which can change the flow characteristics of the gas. At this point, water just like a wall that obstructs the flow of gas. There must be an additional pressure gradient to overcome the resistance of the adsorption layer, as shown in Figure 1. We call this pressure gradient as the threshold pressure gradient (TPG) of gas flow [26].

However, the previously modeling efforts did not consider the impact of TPG on the development of CBM. Some scholars have noticed TPG when they research fluid flow in pore systems [27–32]. Miller and Low firstly introduced the conception of TPG when he studied the mechanism of water flow in clay systems [31]. He figured that the threshold gradient needs to be overcome for water flow. Furthermore, some researchers held that the TPG phenomena for gas flow are explicit in ultra-low-permeability reservoirs, especially when water also exists in the flow path. Tian et al. performed the TPG experimental investigations using the air bubble method, and the results showed that the TPG exists at the connate water saturation, and increases exponentially with either an increase in

TABLE 1: Some geological information of the Nos. 3 and 15 coal seams.

Erathem	System	Formation	Formation thickness	Coal seam thickness
Paleozoic	Lower permian	Lower shihezi	40–110 m	—
		Shanxi	30–70 m	No. 3: 4–6.6 m
	Upper carboniferous	Taiyuan	80–130 m	No. 15: 2.2–10 m
		Middle carboniferous	Benxi	0–45 m

dimensionless water saturation or decrease in permeability [33]. In our previous work, according to the experimental results, it can be concluded that containing water is the prerequisite of the existence of TPG for gas flow in porous media. TPG increases with higher water saturation and lower absolute permeability [32–34].

In this paper, the effect of gas TPG and desorption on an effective control radius of the CBM reservoir with different water saturation is studied by experiment and theoretical analysis. Firstly, we established a new flow model of CBM considering the TPG and gas diffusion. Secondly, we carried out a series of experiments to fit out the gas TPG expression. Then we analyzed the influence of TPG and desorption on the control radius. Finally, we have conducted a case study to analyze the utilization control radius of the target area. This study provides a quick and reasonable prediction of control radius in CBM reservoir different water saturation for further adjustment suggestions and sustainable development.

2. Study Area and Geological Background

China is not only a country of high coal production and consumption but also a country with abundant CBM resources. The block in this paper is located in certain basin in the southeast of Shanxi Province in China as shown in Figure 2 [35]. Since 2011, the block has been explored for CBM development. The common well types in these areas are vertical well.

In this block, two important and productive coal seams for CBM recovery are the No. 3 coal seam from Shanxi Formation and No. 15 coal seam from Taiyuan Formation. Some geological details about both coal seams are summarized in Table 1. Laboratory tests show that the average permeability of Nos. 3 and 15 coal seams in this block are around 0.06 mD and 0.01 mD respectively, indicating low-permeability traits for both coal seams. The initial water saturation of Nos. 3 and 15 coal seams are about 15.6% and 36.9% separately. According to statistical data from appraisal wells in the target block, the No. 3 coal seam contributes more to the overall CBM development than the No. 15 coal seam. Therefore, in this study, the No. 3 coal seam is selected as the target coal seam for the investigation of control radius in two study areas.

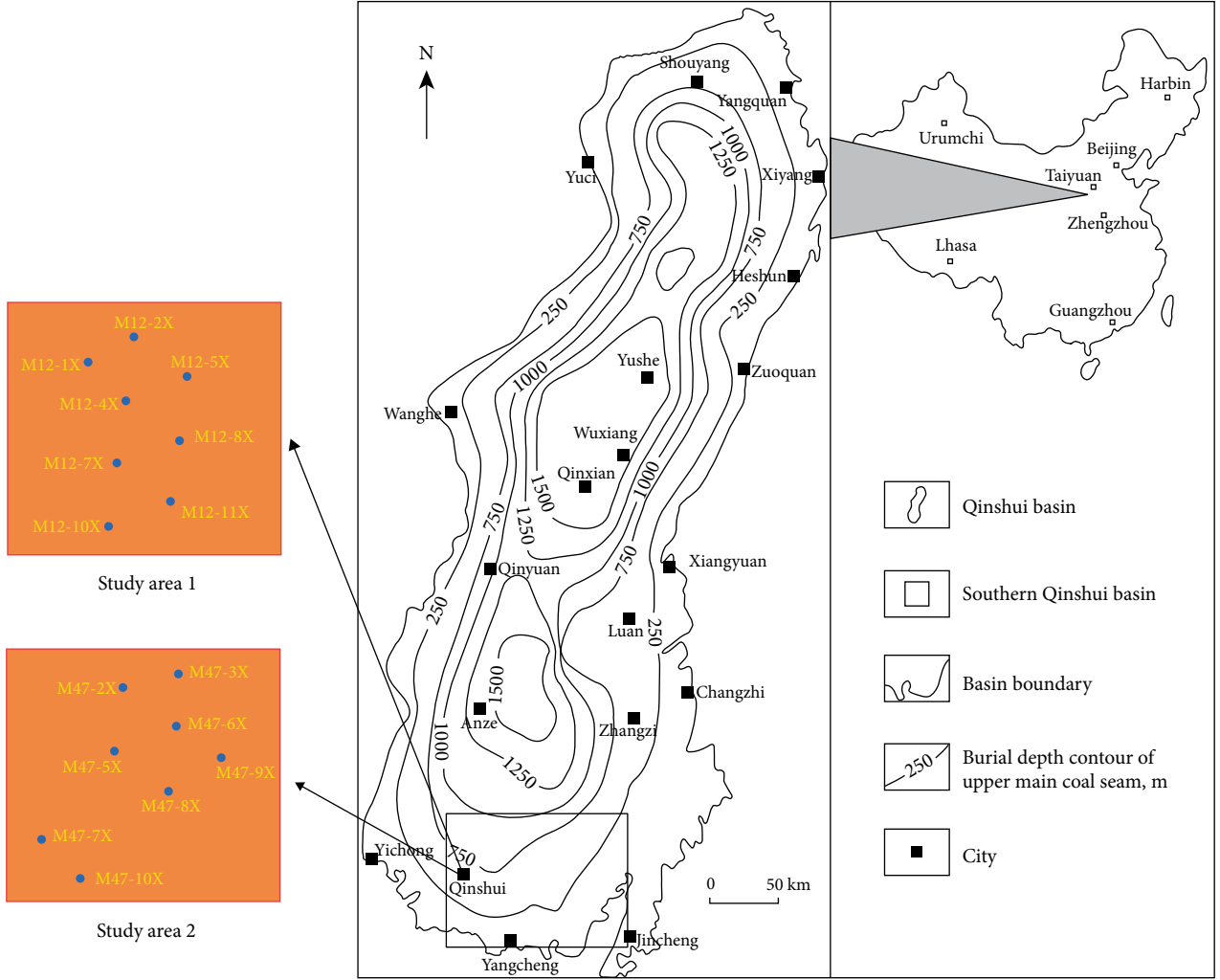


FIGURE 2: Location of the target block in China and two study areas with corresponding wells distributions.

3. Mathematical Model

3.1. Governing Equation. To simplify the model, it is assumed that water is standing. The mathematical model describing the whole process of nonDarcy flow for single-phase gas flow considering desorption is presented as follows [26]:

Mass conservation equation:

$$\frac{\partial}{\partial t}(\rho_g \phi) + \text{div}(\rho_g \vec{v}) - q_d = 0, \quad (1)$$

Motion equation:

$$\vec{v} = \frac{k}{\mu} (\nabla p - G_g), \quad (2)$$

Real gas state equation:

$$pV = nZRT, \quad (3)$$

where Z is the compressibility factor, which is a function of temperature T and volume V . k is permeability, μ is the viscosity of gas, ρ_g is the density of gas, ϕ is porosity, p is the pressure of the reservoir, G_g is the TPG of gas, and q_d is the adsorption of gas.

According to Equations (3), the density of the gas is expressed as follows:

$$\rho_g = \frac{pM}{RTZ}. \quad (4)$$

Similarly, the gas density under standard condition is

$$\rho_{gsc} = \frac{p_{sc}M}{RT_{sc}Z_{sc}}. \quad (5)$$

Substituting Equations (5) into (4), we obtain

$$\rho_g = \frac{T_{sc}Z_{sc}\rho_{gsc}}{p_{sc}} \cdot \frac{p}{TZ}. \quad (6)$$

Isothermal compressibility of gas is defined as

$$C_p = \frac{-(dV/V)}{dp} = -\frac{1}{V} \cdot \frac{dV}{dp} = \frac{1}{p} - \frac{1}{Z} \cdot \frac{\partial Z}{\partial p}. \quad (7)$$

Combining with Equation (6) and (7), the time term of Equation (1) can be expressed as

$$\begin{aligned}\frac{\partial(\rho_g \phi)}{\partial t} &= \frac{T_{sc} Z_{sc} \rho_{gsc} \phi}{p_{sc} T} \left[\frac{1}{p} - \frac{1}{Z(p)} \cdot \frac{\partial Z(p)}{\partial p} \right] \cdot \frac{p}{Z(p)} \frac{\partial p}{\partial t} \\ &= \frac{T_{sc} Z_{sc} \rho_{gsc} \phi \mu(p)}{p_{sc} T} C_\rho \cdot \frac{p}{\mu(p) Z(p)} \frac{\partial p}{\partial t}.\end{aligned}\quad (8)$$

Similarly, according to Equation (2), the second term of Equation (1) in the x direction can be expressed as [26]

$$\begin{aligned}\frac{\partial(\rho_g v_x)}{\partial x} &= \frac{\partial}{\partial x} \left[\frac{T_{sc} Z_{sc} \rho_{gsc}}{p_{sc}} \cdot \frac{p}{TZ} \cdot \frac{k}{\mu(p)} \left(\frac{\partial p}{\partial x} - G_g \right) \right] \\ &= \frac{T_{sc} Z_{sc} \rho_{gsc} k}{p_{sc} T} \left[\frac{\partial}{\partial x} \left[\frac{p}{\mu(p) Z(p)} \cdot \frac{\partial p}{\partial x} \right] - G_g \cdot C_\rho \frac{p}{\mu(p) Z(p)} \cdot \frac{\partial p}{\partial x} \right].\end{aligned}\quad (9)$$

Introducing pseudo-pressure function,

$$m = 2 \int_0^p \frac{p}{\mu(p) Z(p)} dp. \quad (10)$$

Then

$$\frac{dm}{dp} = 2 \cdot \frac{p}{\mu(p) Z(p)}. \quad (11)$$

For convenient engineering applications, $\mu(p)Z(p)$ in Equation (11) can be replaced by μZ , which is the value of $\mu(p)Z(p)$ under average pressure and constant temperature. Then, integrating Equation (11), we obtain

$$m = \frac{1}{\mu Z} \cdot p^2. \quad (12)$$

Substituting Equation (11) into Equation (8), we have

$$\frac{\partial(\rho_g \phi)}{\partial t} = \frac{1}{2} \cdot \frac{T_{sc} Z_{sc} \rho_{gsc} \phi \mu(p)}{p_{sc} T} C_\rho \cdot \frac{\partial m}{\partial t}. \quad (13)$$

Substituting Equation (11) into Equation (9), we have

$$\frac{\partial(\rho_g v_x)}{\partial x} = \frac{1}{2} \cdot \frac{T_{sc} Z_{sc} \rho_{gsc} k}{p_{sc} T} \left[\frac{\partial^2 m}{\partial x^2} - G_g \cdot C_\rho \frac{\partial m}{\partial x} \right]. \quad (14)$$

Similarly, the following formulas in the y and z directions are obtained

$$\frac{\partial(\rho_g v_y)}{\partial y} = \frac{1}{2} \cdot \frac{T_{sc} Z_{sc} \rho_{gsc} k}{p_{sc} T} \left[\frac{\partial^2 m}{\partial y^2} - G_g \cdot C_\rho \frac{\partial m}{\partial y} \right]. \quad (15)$$

$$\frac{\partial(\rho_g v_z)}{\partial z} = \frac{1}{2} \cdot \frac{T_{sc} Z_{sc} \rho_{gsc} k}{p_{sc} T} \left[\frac{\partial^2 m}{\partial z^2} - G_g \cdot C_\rho \frac{\partial m}{\partial z} \right]. \quad (16)$$

When the Hamilton operator and Laplace operator are introduced, we have

$$\begin{aligned}\frac{\partial(\rho_g v_x)}{\partial x} + \frac{\partial(\rho_g v_y)}{\partial y} + \frac{\partial(\rho_g v_z)}{\partial z} - q_d \\ = \frac{1}{2} \cdot \frac{T_{sc} Z_{sc} \rho_{gsc} k}{p_{sc} T} \left[\nabla^2 m - C_\rho G_g \nabla m \right] - q_d.\end{aligned}\quad (17)$$

According to Equation (13) and (17), Equation (1) can be transformed into

$$-(\nabla^2 m - C_\rho G_g \nabla m) + \frac{2 p_{sc} T}{T_{sc} Z_{sc} \rho_{gsc} k} q_d = \frac{\phi \mu(p) C_\rho}{k} \cdot \frac{\partial m}{\partial t}. \quad (18)$$

The gas pressure derivative is defined as

$$\eta = \frac{k}{\phi \mu(p) C_\rho}. \quad (19)$$

Then

$$-\nabla^2 m + C_\rho G_g \nabla m + \frac{2 p_{sc} T}{T_{sc} Z_{sc} \rho_{gsc} k} q_d = \frac{1}{\eta} \frac{\partial m}{\partial t}. \quad (20)$$

3.2. Analytical Solution of Nondarcy Radial Flow. Assuming that $G_c = C_\rho G_g$ for steady plane radial flow, Equation (20) can be transformed into following ordinary differential equations

$$\frac{d^2 m}{dr^2} + \frac{1}{r} \cdot \frac{dm}{dr} - G_c \frac{dm}{dr} - \frac{2 p_{sc} T}{T_{sc} Z_{sc} \rho_{gsc} k} q_d = 0. \quad (21)$$

Equations of constant pressure boundary conditions are given as follows.

$$\begin{aligned}r &= r_w, \\ m &= m_w \\ r &= r_e, \\ m &= m_e.\end{aligned}\quad (22)$$

Combining with Equation (22), the analytical solution of Equation (21) can be obtained.

$$m(r) = -\frac{q_d^* \ln(G_c \cdot r)}{G_c^2} - \frac{q_d^* r}{G_c} - C_1 E_i(G_c \cdot r) + C_2, \quad (23)$$

where

$$\begin{aligned}q_d^* &= \frac{2 p_{sc} T}{T_{sc} Z_{sc} \rho_{gsc} k} \cdot q_d, \\ C_1 &= \frac{(m_e - m_w) G_c^2 + q_d^* \cdot \ln(r_e/r_w) + q_d^* \cdot G_c (r_e - r_w)}{G_c^2 \cdot (E_i(G_c \cdot r_w) - E_i(G_c \cdot r_e))}, \\ C_2 &= m_w + \frac{q_d^* \ln(G_c \cdot r_w)}{G_c^2} + \frac{q_d^* r_w}{G_c} + C_1 \cdot E_i(G_c \cdot r_w).\end{aligned}\quad (24)$$

According to Equation (12), $m_e = (1/\mu Z) \cdot p_e^2$ and $m_w = (1/\mu Z) \cdot p_w^2$, the pressure distribution is shown as Equation (25).

$$p(r) = \sqrt{\left(-\frac{q_d^* \ln(G_c \cdot r)}{G_c^2} - \frac{q_d^* r}{G_c} - C_1 E_i(G_c \cdot r) + C_2 \right) \cdot \mu Z}. \quad (25)$$

According to Equation (25), we can obtain the formation pressure gradient. Comparing with the gas TPG, when $dp/dr = G_g$, the corresponding radius will be equal to the control radius.

TABLE 2: Parameters of formation water from the No. 3 coal seam.

Na ⁺ +K ⁺	Mg ²⁺	Ion concentration, mg/L				HCO ₃ ⁻	Total salinity, mg/L	Water type
		Ca ²⁺	Cl ⁻	SO ₄ ²⁻				
488.16	3.98	4.82	245.59	17.83	884.93	1645.31	NaHCO ₃	

TABLE 3: The permeability and water saturation of the cores for the two groups of experiments.

TPG with permeability (with the same water saturation)									
Core number	1	2	3	4	5	6	7	8	9
Permeability (mD)	0.023	0.036	0.043	0.052	0.140	0.154	0.188	0.251	0.326
TPG with water saturation (with the same permeability)									
Core number	1	2	3	4	5	6	7	8	
Water saturation (%)	15.24	24.56	30.26	35.30	42.10	46.82	52.81	56.18	

4. Experimental Study

Due to the existence of TPG, gas–water two-phase flow shows typical low-velocity nonDarcy flow characteristics [21–23]. In this paper, we designed experiments to validate and obtain the relationship between TPG and the permeability, water saturation.

4.1. Experimental Method and Procedures. The coal core samples were obtained from the No. 3 coal seam in the study area. The diameter of each core sample is 2.5 cm on average, and the length ranges from 4.5 cm to 6 cm. In this paper, the porosity and the permeability of coal samples were measured using a fully automatic pore-permeability simultaneous measuring instrument. The permeability in this paper is gas log permeability. The average porosity for core samples of No. 3 coal seam is 4.3%. The gas used in this experiment was methane with a purity of more than 99.99%. The water was prepared in the laboratory according to some actual parameters of formation water from No. 3 coal seam, as shown in Table 2. After that, we use special core displacement equipment to inject gas into the different permeability cores with different water saturation, and calculate the influence of water cut and permeability on gas injection displacement by recording gas production rate, then determine the TPG of coal-cores with water, the parameters of two groups of experiments are shown in Table 3. Figure 3 shows the schematic of the experimental equipment and core samples.

4.2. Experimental Results. In the experiments, we have obtained the gas flow rate under different permeability and water saturation. Figure 4(a) shows the relationship between the gas flow rate and the pressure square difference under different permeability. With the results, we calculated the gas TPGs under different permeability as shown in Figure 4(b) (blue points), and then obtained the fitting curve and the new fitting formula as shown in Equation (26). The results show that TPG is negatively correlated with permeability, and the larger the permeability, the smaller the TPG. In the same

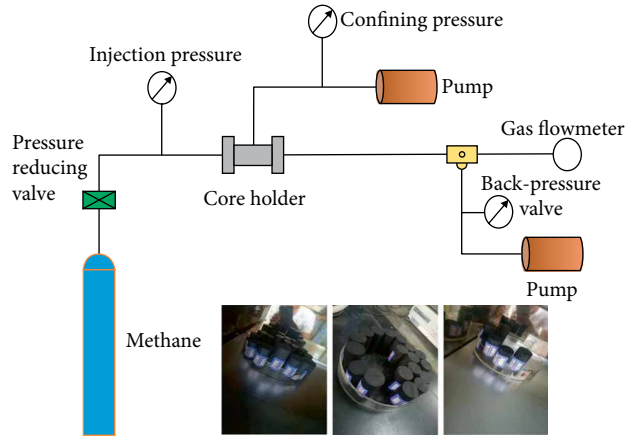


FIGURE 3: Schematic of TPG experimental equipment and core samples.

way, we obtained the fitting curve as shown in Figure 5, and the new fitting formula of the relationship between gas TPG and water saturation as shown in Equation (27). The results show that TPG is positively correlated with water saturation. It also can be found that the fitting formulas match the data distribution perfectly, and all the correlative factors (R^2) are above 0.9.

$$G_g = cS_w^d = 0.0053S_w^{1.2923}. \quad (26)$$

$$G_g = aK^b = 0.1345K^{-0.641}. \quad (27)$$

According to the analysis and fitting of the test results, the relationship between gas TPG and permeability, water saturation of high-rank coal seams in the target block is shown in Equation (28).

$$G_g = 0.6556 \cdot K^{-1.131} \cdot S_w^{3.27} + 0.2381. \quad (28)$$

Combining Equation (28) and Equation (25), we can obtain new pressure function, as shown in Equation (29).

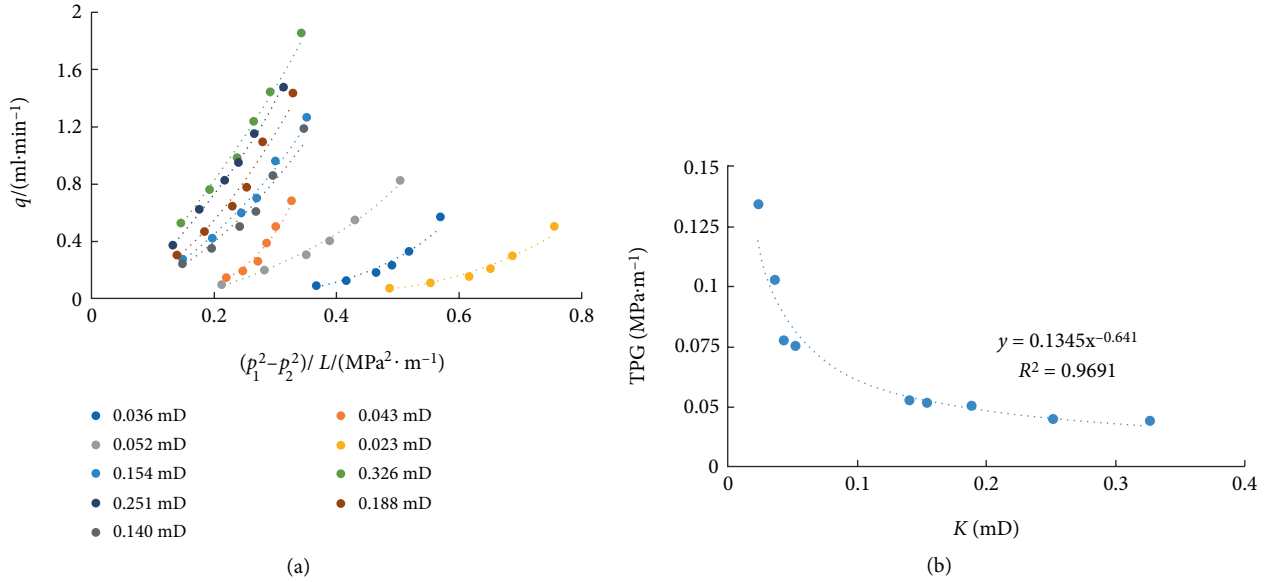


FIGURE 4: (a) Relationship between gas flow rate and pressure square difference under different permeability. (b) The correlation between permeability and TPG.

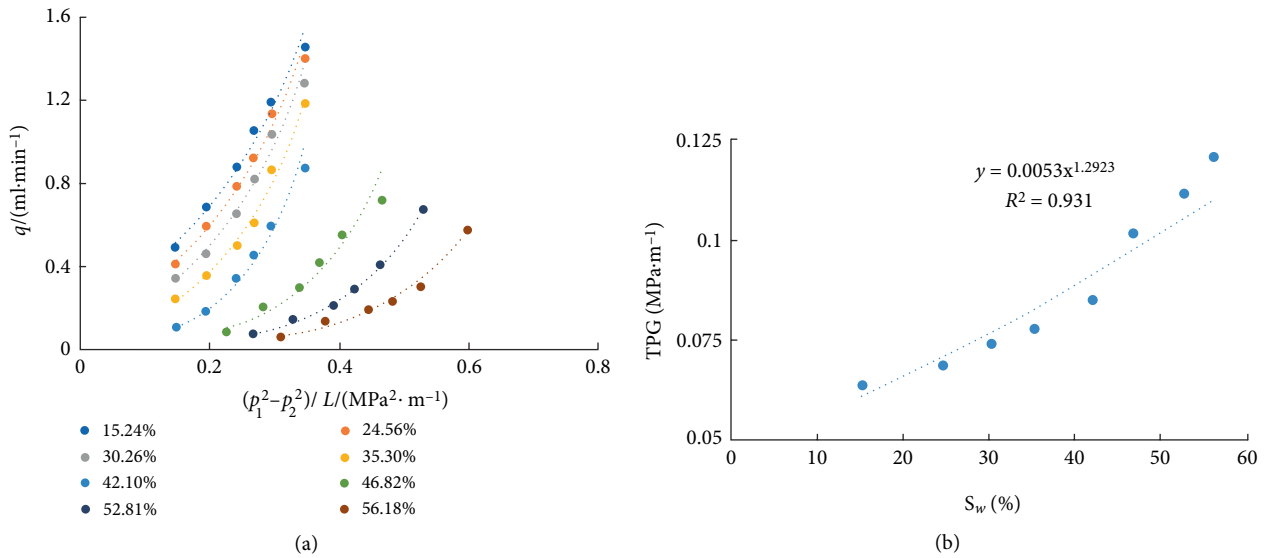


FIGURE 5: (a) Relationship between gas flow rate and pressure square difference under different water saturation. (b) The correlation between water saturation and TPG.

$$p(r) = \sqrt{\left(\frac{q_d^* \ln \left((C_p 0.6556 \cdot K^{-1.131} \cdot S_w^{3.27} + 0.2381) \cdot r \right)}{(C_p 0.6556 \cdot K^{-1.131} \cdot S_w^{3.27} + 0.2381)^2} - \frac{q_d^* r}{C_p 0.6556 \cdot K^{-1.131} \cdot S_w^{3.27} + 0.2381} - C_1 E_i \left((C_p 0.6556 \cdot K^{-1.131} \cdot S_w^{3.27} + 0.2381) \cdot r \right) + C_2 \right) \cdot \bar{\mu} Z}. \quad (29)$$

5. Results and Discussion

5.1. Calculation Parameters. In this paper, we compare the pressure distribution of the target block with the present model under the same reservoir condition. The result shows that the present model has good agreement with the field test data. After that, we analyzed the influence of TPG and desorption on formation pressure and drainage radius, and obtain the effective utilization of reservoirs with different

water saturation. The basic parameters used in the calculation process are all from the real values of the target block, which are shown in Table 4.

5.2. Effect of TPG. Figure 6(a) shows the relationship between the formation pressure and the drainage radius under different gas TPG. Figure 6(b) is the relationship between formation pressure gradient and drainage radius. The results show that the control radius is increased with the decrease of TPG, the

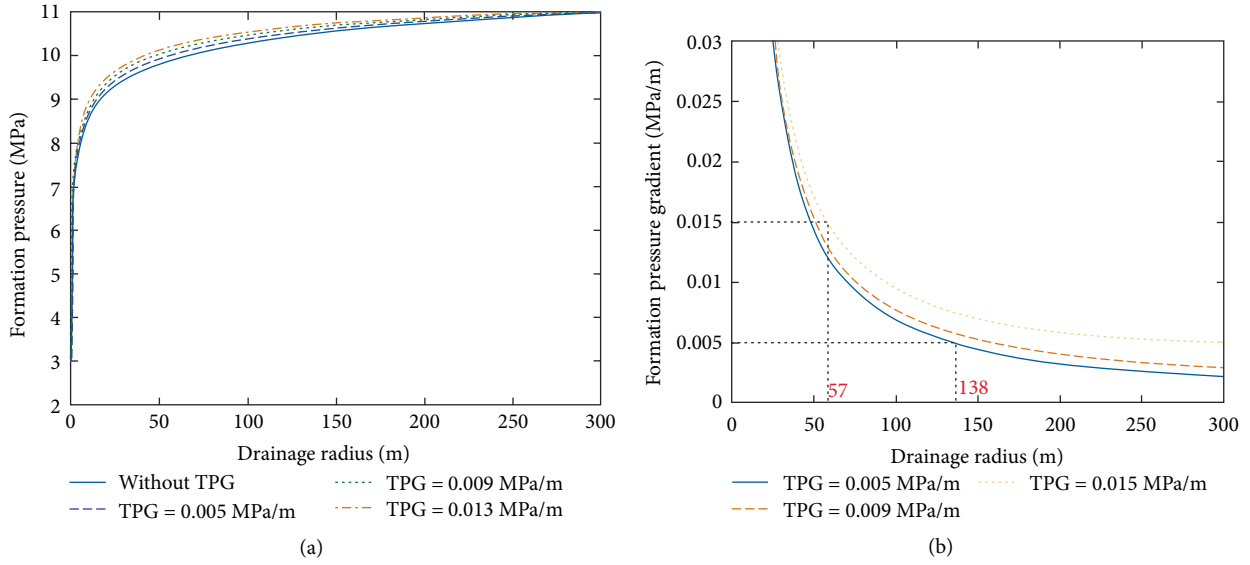


FIGURE 6: Effect of TPG on formation pressure and formation pressure gradient. (a) Relationship between formation pressure and drainage radius under different TPG. (b) Relationship between formation pressure gradient and drainage radius under different TPG.

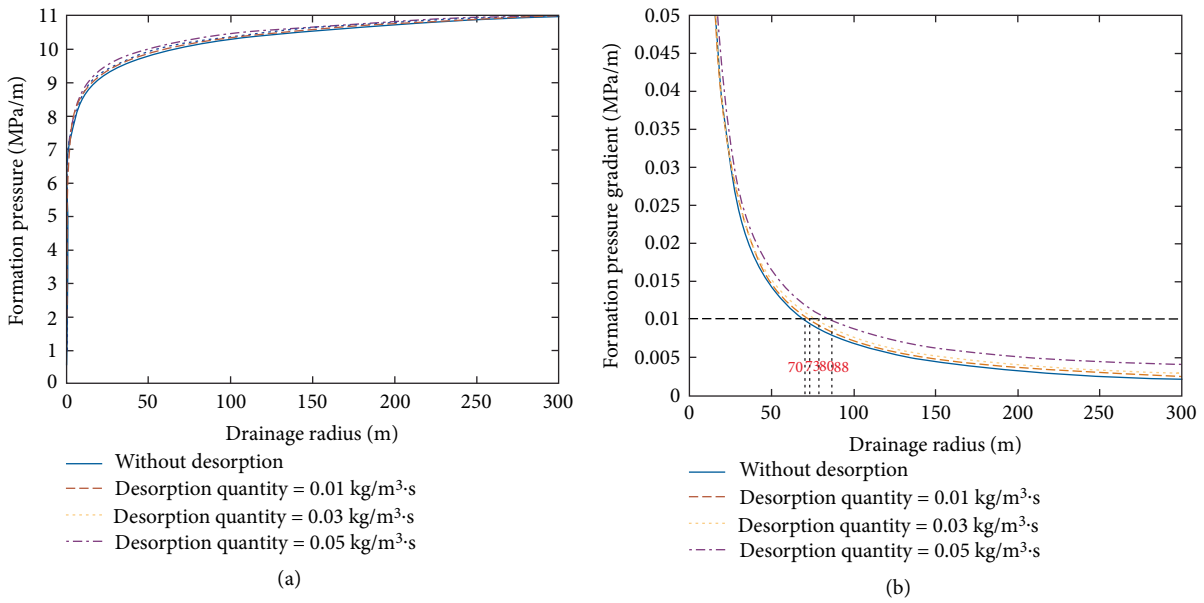


FIGURE 7: Effect of desorption on formation pressure and formation pressure gradient. (a) Relationship between formation pressure and drainage radius under different desorption quantity. (b) Relationship between formation pressure gradient and drainage radius under different desorption quantity.

TABLE 4: The basic parameters of the target block.

Parameters	Value (unit)
The formation pressure p_e	10 (MPa)
The production well pressure p_w	3 (MPa)
Isothermal compression coefficient C_p	0.01 (MPa ⁻¹)
Gas viscosity μ	0.028 (mPa·s)
Compressibility factor Z	0.89
The radius of pressure relief r_e	300 (m)
The radius of the wellbore r_w	0.1 (m)
Desorption amounts q_d	0.03 (kg/(m ³ s))

TABLE 5: The classification standard of wells based on control radius.

Control radius (m)	Well classification
<50	V
50~80	IV
80~100	III
100~120	II
>120	I

TABLE 6: The parameters and the calculation results of two study areas.

Study area	Well number	P_e (MPa)	P_w (MPa)	S_w (%)	TPG (MPa/m)	Control radius	Well classification
Study area 1	1	9.58	5.57	6.4	0.0057	136.7	I
	2	9.72	5.37	11.6	0.0087	87.5	III
	3	9.84	5.02	15	0.0115	55	IV
	4	9.89	5.35	9.5	0.0074	103.6	II
	5	9.96	5.85	12.5	0.0094	87.1	III
	6	9.91	5.92	11.5	0.0087	93.7	III
	7	10	5.06	9.4	0.0073	101.4	II
	8	10.01	5.13	11.8	0.0089	80.6	III
Study area 2	1	9.09	4.11	9.1	0.0071	85.7	III
	2	9.5	5.24	6.5	0.0058	112.5	II
	3	9.22	5.7	11.5	0.0087	91.3	III
	4	9.01	4.21	9.1	0.0071	87.2	III
	5	9.4	5.44	12.3	0.0093	82.2	III
	6	9.04	4.59	11.8	0.0089	79.6	IV
	7	9.43	4.93	9.1	0.0071	91.6	III
	8	9.44	5.65	12.1	0.0091	85.7	III

bigger of the TPG, the smaller the pressure drop rate. When the TPG is 0.005~0.015 MPa/m, the control radius is from 57 m to 138 m, which guides the development and the design of well pattern layout.

5.3. Effect of Desorption. In this section, we analyzed the influence of desorption effect and the desorption quantity on the control radius. Figure 7(a) is the relationship between the formation pressure and the drainage radius under different desorption quantity. And Figure 7(b) shows the relationship between formation pressure gradient and drainage radius. The result shows that the desorption effect slows down the rate of pressure reduction. In addition, comparing with control radius without desorption effect, the promotion efficiency is 4.3%, 14.3%, and 25.7% when the desorption quantity is $0.01 \text{ kg/m}^3 \cdot \text{s}$, $0.03 \text{ kg/m}^3 \cdot \text{s}$ and $0.05 \text{ kg/m}^3 \cdot \text{s}$ respectively. It can be concluded that the existence of desorption promotes the sustainable development of CBM.

5.4. Control Radius of the Target Well Groups. In order to distinguish the production capacity of gas wells and facilitate the adjustment of production measures in the later period production, wells are classified based on the control radius in the field production process of the target block. The specific classification standard is shown in Table 5.

We calculated the effective control radius of two typical vertical well groups in the target block using the present model, which has 8 wells for each well group. Then classified the wells according to Table 5. The results are shown in Table 6. The values of G_g in the table are obtained through core experiments.

By analyzing the results in Table 6, we can know that the control radius of these two blocks is mainly distributed in III (80~100 m). The average control radius is 91.3 m, the average

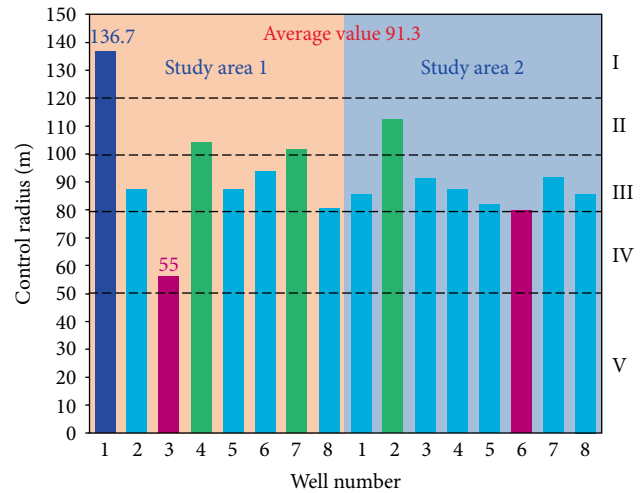


FIGURE 8: The histogram of the control radius distribution.

gas TPG is 0.0082 MPa/m. From Table 6 it can be also proved that the lower the water saturation, the larger the control radius, which will be better development effects. Figure 8 is the histogram of the control radius distribution. From the figure, we can obtain that the effective utilization of study area 1 is better than study area 2.

In order to analyze the utilization of the target area more intuitively, we calculated and drew the isogram of the control radius based on the actual well location as shown in Figure 9. The results indicate the utilization scope of the target and provide the basis for later adjustment measures. For example, in order to increase the utilization area and sustainable development ability we can use well pattern infilling in region II and III based on engineering practices. For region IV, the control radius can be increased by hydraulic fracturing.

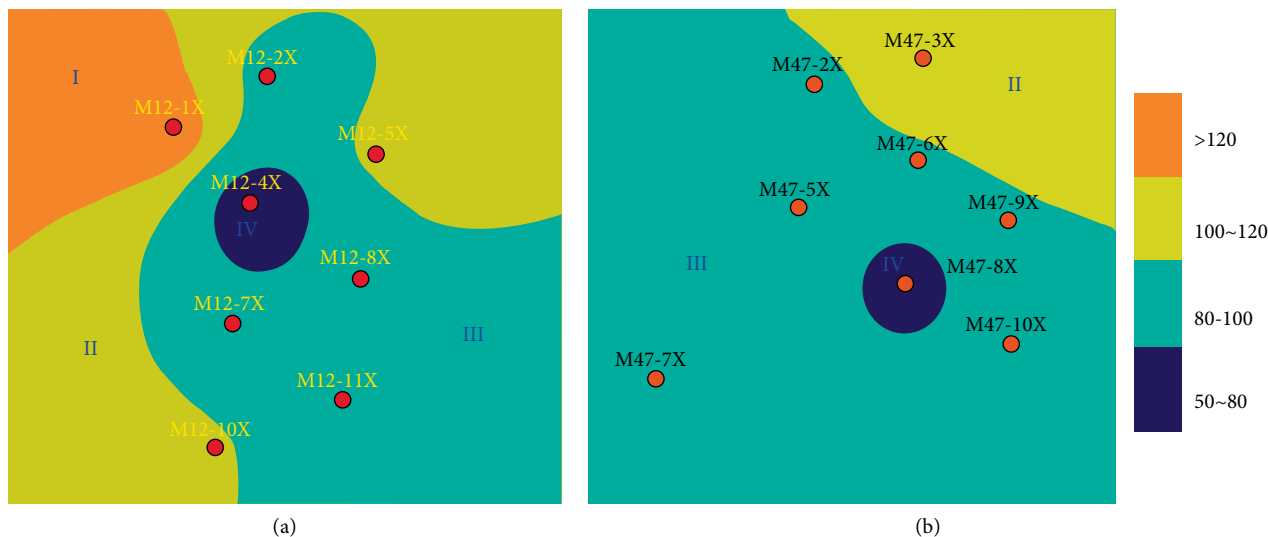


FIGURE 9: The isogram of the control radius. (a) Study area 1. (b) Study area 2.

6. Conclusion

In this paper, a new flow model of CBM with different water saturation has been established considering the TPG and gas desorption. We have obtained the pressure distribution and control radius of CBM reservoirs. After that, we carried out a series of experiments to study the relationship between TPG and permeability and water saturation and fitted out the new relational expression between them. Then, we analyzed the influence of TPG and desorption on the control areas and the sustainable development ability. Finally, we selected 2 well groups from the target block to analyze the actual utilization situation using the present model.

The results show that the present model has good agreement with the field test data. The control radius is increased with the decrease of TPG, the bigger of the TPG, the smaller the pressure drop rate. Besides, the desorption effect slows down the rate of pressure reduction, and the promotion efficiency is 25.7% when the desorption quantity is $0.05 \text{ kg/m}^3 \cdot \text{s}$.

Through the case study, we obtain that the control radius of target well groups ranges from 55 m to 136.7 m. The average control radius and gas TPG are 91.3 m 0.0082 MPa/m respectively. In addition, the lower the water saturation is, and the larger the control radius is. After that, we classify the wells into 5 categories according to the control radius, which is mainly distributed in III (80~100 m). Based on engineering practices, we suggest using well pattern infilling to increase the utilization area in region II and III, and utilizing hydraulic fracturing method for region IV.

This study provides a quick and reasonable prediction of control radius for the CBM reservoir with different water saturation and gives guidance for further adjustment measures and sustainable development.

Data Availability

The data used to support the findings of this study are included in the article.

Conflicts of Interest

The authors declare that they have no conflicts of interest.

Acknowledgments

We gratefully acknowledge the National Science and Technology Major Project (Grant No. 2017ZX05064-001 and No. 2016ZX05041-002) for financial support.

References

- [1] S. Tao, S. Chen, and Z. Pan, "Current status, challenges, and policy suggestions for coalbed methane industry development in China: a review," *Energy Science & Engineering*, 2019.
- [2] S. Tao, Z. J. Pan, S. L. Tang, and S. D. Chen, "Current status and geological conditions for the applicability of CBM drilling technologies in China: a review," *International Journal of Coal Geology*, vol. 202, pp. 95–108, 2019.
- [3] H. Jianchao, W. Zhiwei, and L. Pingkuo, "Current states of coalbed methane and its sustainability perspectives in China," *International Journal of Energy Research*, vol. 42, no. 11, pp. 3454–3476, 2018.
- [4] U. Singh and L. M. Colosi, "Water–energy sustainability synergies and health benefits as means to motivate potable reuse of coalbed methane-produced waters," *Ambio*, vol. 48, no. 7, pp. 752–768, 2019.
- [5] X. Luo, X. Zhang, L. Zhang, and G. Huang, "Visualization of chinese CBM research: a scientometrics review," *Sustainability*, vol. 9, no. 6, pp. 980–991, 2017.
- [6] H. Aljamaan, R. Holmes, V. Vishal, R. Haghpanah, J. Wilcox, and A. R. Kavscek, "CO₂ storage and flow capacity measurements on idealized shales from dynamic breakthrough experiments," *Energy & Fuels*, vol. 31, no. 2, pp. 1193–1207, 2017.
- [7] R. Holmes, E. C. Rupp, V. Vishal, and J. Wilcox, "Selection of shale preparation protocol and outgas procedures for applications in low-pressure analysis," *Energy & Fuels*, vol. 31, no. 9, pp. 9043–9051, 2017.

- [8] P. Psarras, R. Holmes, V. Vishal, and J. Wilcox, "Methane and CO₂ adsorption capacities of kerogen in the eagle ford shale from molecular simulation," *Accounts of Chemical Research*, vol. 50, no. 8, pp. 1818–1828, 2017.
- [9] B. Hazra, D. A. Wood, V. Vishal, and A. K. Singh, "Pore characteristics of distinct thermally mature shales: influence of particle size on low-pressure CO₂ and N₂ adsorption," *Energy & Fuels*, vol. 32, no. 8, pp. 8175–8186, 2018.
- [10] M. Pillalamarry, S. Harpalani, and S. Liu, "Gas diffusion behavior of coal and its impact on production from coalbed methane reservoirs," *International Journal of Coal Geology*, vol. 86, pp. 342–348, 2011.
- [11] S. Tao, S. Chen, D. Tang, X. Zhao, H. Xu, and S. Li, "Material composition, pore structure, and adsorption capacity of low-rank coals around the first coalification jump: a case of eastern junggar basin, China," *Fuel*, vol. 211, pp. 804–815, 2018.
- [12] M. G. Yun, M. W. Rim, and C. N. Han, "A model for pseudo-steady and non-equilibrium sorption in coalbed methane reservoir simulation and its application," *Journal of Natural Gas Science and Engineering*, vol. 54, pp. 342–348, 2018.
- [13] T. Li, H. Song, J. Wang, Y. Wang, and J. Killough, "An analytical method for modeling and analysis gas-water relative permeability in nanoscale pores with interfacial effects," *International Journal of Coal Geology*, vol. 159, pp. 71–81, 2016.
- [14] J. Wang, H. Song, V. Rasouli, and J. Killough, "An integrated approach for gas-water relative permeability determination in nanoscale porous media," *Journal of Petroleum Science and Engineering*, vol. 173, pp. 237–245, 2019.
- [15] J. Zhao, D. Tang, H. Xu, Y. Lv, and S. Tao, "High production indexes and the key factors in coalbed methane production: a case in the hancheng block, southeastern Ordos Basin, China," *Journal of Petroleum Science and Engineering*, vol. 130, pp. 55–67, 2015.
- [16] Y. Lv, D. Tang, H. Xu, and H. Luo, "Production characteristics and the key factors in high-rank coalbed methane fields: a case study on the fanzhuang block, Southern Qinshui basin, China," *International Journal of Coal Geology*, vol. 96, pp. 93–108, 2012.
- [17] J. G. Wang, J. Liu, and A. Kabir, "Combined effects of directional compaction, non-Darcy flow and anisotropic swelling on coal seam gas extraction," *International Journal of Coal Geology*, vol. 109, pp. 1–14, 2013.
- [18] B. Gong, Y. Zhang, Y. Fan, and G. Qin, "A novel approach to model enhanced coal bed methane recovery with discrete fracture characterizations in a geochemical simulator," *Journal of Petroleum Science and Engineering*, vol. 124, pp. 198–208, 2014.
- [19] V. Vishal, T. N. Singh, and P. G. Ranjith, "Influence of sorption time in CO₂-ECBM process in indian coals using coupled numerical simulation," *Fuel*, vol. 139, pp. 51–58, 2015.
- [20] H. Song, M. Yu, W. Zhu et al., "Numerical investigation of gas flow rate in shale gas reservoirs with nanoporous media," *International Journal of Heat and Mass Transfer*, vol. 80, pp. 626–635, 2015.
- [21] S. Chen, T. Yang, P. G. Ranjith, and C. Wei, "Mechanism of the two-phase flow model for water and gas based on adsorption and desorption in fractured coal and rock," *Rock Mechanics and Rock Engineering*, vol. 50, pp. 571–586, 2017.
- [22] B. Lin and C. Shen, "Coal permeability-improving mechanism of multilevel slotting by water jet and application in coal mine gas extraction," *Environmental Earth Sciences*, vol. 73, no. 10, pp. 5975–5986, 2015.
- [23] T. Q. Xia, F. Gao, J. H. Kang, and X. X. Wang, "A fully coupling coal-gas model associated with inertia and slip effects for CBM migration," *Environmental Earth Sciences*, vol. 75, no. 7, pp. 582–591, 2016.
- [24] P. Liu, Y. Qin, S. Liu, and Y. Hao, "Non-linear gas desorption and transport behavior in coal matrix: experiments and numerical modeling," *Fuel*, vol. 214, pp. 1–13, 2018.
- [25] Z. Sun, J. Shi, T. Zhang et al., "A fully-coupled semi-analytical model for effective gas/water phase permeability during coalbed methane production," *Fuel*, vol. 23, pp. 44–52, 2018.
- [26] G. Huang, H. Song, Y. Cao et al., "Numerical investigation of low-velocity non-Darcy flow of gas and water in coal seams," *Journal of Natural Gas Science and Engineering*, vol. 34, pp. 124–138, 2016.
- [27] W. Tian, A. Li, X. Ren, and Y. Josephine, "The threshold pressure gradient effect in the tight sandstone gas reservoirs with high water saturation," *Fuel*, vol. 226, pp. 221–229, 2016.
- [28] Y. Zhang, J. Zeng, J. Qiao, X. Feng, F. Wang, and N. Ren, "Experimental study on natural gas migration and accumulation mechanism in sweet spots of tight sandstones," *Journal of Natural Gas Science and Engineering*, vol. 36, pp. 669–678, 2016.
- [29] T. Teng, J. G. Wang, F. Gao, Y. Ju, and T. Xia, "Impact of water film evaporation on gas transport property in fractured wet coal seams," *Transport in Porous Media*, vol. 113, no. 2, pp. 357–382, 2016.
- [30] X. Wang and J. J. Sheng, "Pore network modeling of the non-Darcy flows in shale and tight formations," *Journal of Petroleum Science and Engineering*, vol. 163, pp. 511–518, 2018.
- [31] R. J. Miller and P. F. Low, "Threshold gradient for water flow in clay systems," *Soil Science Society of America Journal*, vol. 27, no. 6, pp. 605–609, 1963.
- [32] W. Zhu, H. Song, X. Huang, X. Liu, D. He, and Q. Ran, "Pressure characteristics and effective deployment in a water-bearing tight gas reservoir with low-velocity non-Darcy flow," *Energy and Fuels*, vol. 25, no. 3, pp. 1111–1117, 2011.
- [33] F. Thauvin and K. K. Mohanty, "Network modeling of non-darcy flow through porous media," *Transport in Porous Media*, vol. 31, no. 1, pp. 19–37, 1998.
- [34] H. Song, Y. Cao, M. Yu, Y. Wang, J. Killough, and J. Leung, "Impact of permeability heterogeneity on production characteristics in water-bearing tight gas reservoirs with threshold pressure gradient," *Journal of Natural Gas Science and Engineering*, vol. 22, pp. 172–181, 2015.
- [35] S. Tao, Y. Wang, D. Tang et al., "Dynamic variation effects of coal permeability during the coalbed methane development process in the qinshui basin, China," *International Journal of Coal Geology*, vol. 93, pp. 16–22, 2012.



Hindawi
Submit your manuscripts at
www.hindawi.com

